

Graph topological transformations in space-filling cell aggregates

Tanmoy Sarkar¹ and Matej Krajnc¹

¹ Jožef Stefan Institute, Jamova 39, SI-1000 Ljubljana, Slovenia

Correspondence and requests for materials should be addressed to M.K. (email: matej.krajnc@ijs.si)

Abstract

Cell rearrangements are fundamental mechanisms driving large-scale deformations of living tissues. In three-dimensional (3D) space-filling cell aggregates, cells rearrange through local topological transitions of the network of cell-cell interfaces, which is most conveniently described by the vertex model. Since these transitions are not yet mathematically properly formulated, the 3D vertex model is generally difficult to implement. The few existing implementations rely on highly customized and complex software-engineering solutions, which cannot be transparently delineated and are thus mostly non-reproducible. To solve this outstanding problem, we propose a reformulation of the vertex model. Our approach, called Graph Vertex Model (GVM), is based on storing the topology of the cell network into a knowledge graph with a particular data structure that allows performing cell-rearrangement events by simple graph transformations. We find these transformations consisting of transformation patterns corresponding to T1 transitions, thereby unifying topological transitions in 2D and 3D space-filling packings. This result suggests that the GVM's graph data structure may be the most natural representation of cell aggregates and tissues. We use GVM to characterize solid-fluid transition in 3D cell aggregates, driven by active noise and find aggregates undergoing efficient ordering close to the transition point. In all, our work showcases knowledge graphs as particularly suitable data models for structured storage, analysis, and manipulation of tissue data, which potentially has paradigm-shifting implications for the fields of tissue biophysics and biology.

The mechanical interactions between individual cells and between the cells and their environment play a crucial role in determining the macroscopic properties and behaviors of animal tissues on a large scale [1–7]. During embryonic development, for example, forces generated within cellular cortices drive precise and highly orchestrated active deformations and collective cellular flows [8–13]. The mechanical forces are transmitted across the tissue through cell-cell contacts, which form a complex spatial network with a dynamically changing topology [14–25].

These cross-scale tissue mechanics have been addressed by computational models that represent cells as discrete entities with certain physical properties that phenomenologically describe the mechanics at smaller length scales [26–35]. Arguably the most widely used and most detailed is the vertex model, which describes individual cells as polygons (2D) or polyhedra (3D) and parametrizes their shapes by vertex positions [36–39]. Mechanical forces on the vertices are typically specified through a model potential energy, which effectively describes complex biomechanics of individual cells using only a small number of model parameters. Simulations of the vertex model include time integration of a system of dynamic equations for the vertices and topological transformations of the network of cell-cell interfaces accompanying cell rearrangements.

Conventional vertex models, which store the topology and geometry of the tissue in a tabular form within arrays, perform topological transformations by updating these arrays according to specified rules [40–43]. Although programming the routines that perform these dynamic array updates is relatively manageable for planar polygonal cell packings and even for 3D surface packings involving polyhedral prism-like cells [44–48], developing computer codes for simulations of 3D bulk cell aggregates poses a significantly greater challenge. Indeed, since the pioneering work by Honda *et al.* [36], who first introduced a vertex model of 3D cell aggregates, there have only been a few recent works reporting successful attempts of coding a full 3D

vertex model with dynamic cell rearrangements [49–51]. The main difficulty lies in the intricate architecture and extensive length of the codes necessary for implementing cell rearrangements with the conventional data model [40–43], which raises questions about its suitability and challenges our basic understanding of rearrangements in space-filling packings.

To address these challenges, we introduce a reformulation of the vertex model called Graph Vertex Model (GVM). We discover a particular graph-data model, which allows formulating topological transformations of cell networks as simple graph transformations. The blueprint outlining the relationships among the components is specified through a metagraph which is designed in a manner that topological transformations are themselves represented by graphs. This design not only enhances their intuitive and visual understanding but also simplifies their implementation, making it accessible even to researchers with limited programming expertise. Furthermore, we show that within the GVM’s data representation, topological transformations in 3D space-filling packings become composites of T1 transitions and they exactly reduce to a single T1 transition when applied to a 2D system. This is a fundamental result that unifies rearrangements in 2D and 3D space-filling packings and suggests that GVM’s data model may be the most natural representation of these systems. As a proof of concept, we develop an open-source Python package `neoVM`, which implements GVM over a graph database, managed in `Neo4j` [52, 53]. We use our new approach to study solid-fluid transition in 3D cell aggregates. We characterize the transition and find aggregates undergoing most efficient ordering in the vicinity of the transition point.

Vertex model. A cell aggregate is represented as a three-dimensional packing of space-filling polyhedral cells (Fig. 1a). Cell shapes are parametrized by positions of vertices in the (x, y, z) space:

$$\mathbf{r}_i = (x_i, y_i, z_i) . \quad (1)$$

Here $i = 1, \dots, N_v$, where N_v is the total number of vertices.

Pairs of vertices are connected by oriented edges, defined by the indices of the constituent vertices:

$$\mathbf{e}_j = \left[+i_j^{(h)}, -i_j^{(t)} \right] . \quad (2)$$

Here $i_j^{(h)}$ and $i_j^{(t)}$ denote indices of head and tail vertices of edge j , respectively (Fig. 1a), and $j = 1, \dots, N_e$, with N_e being the total number of edges. The signs of the vertex indices, $s_j^{(h/t)} = \pm 1$ denotes head and tail vertices of the edge. While at this point these signs seem redundant, since the order in which the indices appear in \mathbf{e}_j itself indicates the head/tail role of the corresponding vertices, they will become important later on.

Polygonal cell sides are defined by oriented lists of indices of their constituent edges as

$$\mathbf{p}_k = \left[\sigma_k^{(\mu)} j_k^{(\mu)} \right]_{\mu=1, \dots, n_k^{(e)}} , \quad (3)$$

where $k = 1, \dots, N_p$, with N_p being the total number of polygons. The $n_k^{(e)}$ edges in the list \mathbf{p}_k are listed sequentially and $\sigma_k^{(\mu)} = \pm 1$ denotes the orientation of the μ -th edge (with index $j_k^{(\mu)}$) within the polygon relative to a chosen positive direction (Fig. 1a).

Similarly, cells are defined by oriented lists of indices of the $n_l^{(p)}$ constituent polygons as

$$\mathbf{c}_l = \left[\Sigma_l^{(\nu)} k_l^{(\nu)} \right]_{\nu=1, \dots, n_l^{(p)}} , \quad (4)$$

where $l = 1, \dots, N_c$, with N_c being the total number of cells within the aggregate. Polygon orientations $\Sigma_l^{(\nu)} = \pm 1$, where -1 and $+1$ correspond to the polygon’s normal vector pointing towards the cell center and away from the cell center, respectively (Fig. 1a). The direction of the polygon’s normal vector is defined by the right-hand-screw rule, where the fingers curl along the chosen polygon’s positive orientation of the bounding edges (Fig. 1a). In contrast to the case of polygons, \mathbf{p}_k , polygon indices in \mathbf{c}_l need not be listed in any specific order.

A couple of exemplary structures of cell aggregates with $N_c = 128$ cells is given in the online repository of `neoVM` [52].

The dynamics of cell-shape changes are described by simulating movements of the vertices, driven by mechanical forces. In a model that neglects inertial effects and only considers friction of vertices with a static ("ether-type") background, vertices follow first-order dynamics described by

$$\eta \frac{d\mathbf{r}_i}{dt} = -\nabla_i W + \mathbf{F}_i^{(a)}. \quad (5)$$

Here the η is the friction coefficient, W is the potential energy of the aggregate, and $\mathbf{F}_i^{(a)}$ is a system-specific active-force contribution. The potential energy is typically calculated from geometric properties of cells such as surface areas of cell-cell contacts A , cell volumes V , etc. These quantities are calculated from the vertex positions as sums over geometric elements, i.e., vertices, edges, polygons (Methods).

Topological transitions. In addition to changing their shapes, cells also change their relative organization within the tissue by exchanging their neighbors [36]. These reorganization events alter the topology of the network of cell-cell contacts, thereby also affecting the interaction between the vertices. In confluent cell aggregates, cells exchange their neighbors by (i) merging vertex pairs of vanishingly short edges and (ii) resolving these vertices into new edges [58–60]. The topology of the edge network after these transformations locally differs from the initial one. In particular, cells that were initially separated might become neighbors, whereas pairs of initially neighboring cells may separate.

To model cell rearrangements in 3D cell aggregates, the following elementary local topological transformations need to be considered (Fig. 1b,c): (i) Edge-to-vertex (EV) transition merges vertices of a vanishingly short edge into a single 6-fold vertex, (ii) vertex-to-triangle (VT) transition resolves a 6-fold vertex into a new triangle, (iii) triangle-to-vertex (TV) transition merges all three vertices of a triangular polygon into a single 6-fold vertex, and (iv) vertex-to-edge (VE) transition resolves a 6-fold vertex into a new edge.

An EV followed by a VT completes an ET transition, which transforms a vanishing edge into a triangle, formed in the perpendicular direction to the shrinking edge (Fig. 1b,c). After an ET transition, initially separated cells become neighbors by sharing the new triangle. Similarly, a TV followed by a VE, completes a TE transition, which transforms a vanishing triangle into an edge, formed in the perpendicular direction to the shrinking triangle (Fig. 1b,c). After a TE transition, the neighboring cells initially sharing the triangle become separated. We note that in a special case of an epithelial monolayer, where cells only attach to their neighbors laterally but not apically and basally, EV transitions either on basal or apical edges give rise to scutoidal cells [61, 62].

Importantly, as illustrated in Fig. 1d, the 4 basic topological transformations are in fact composites of multiple edge-to-vertex and vertex-to-edge transitions, known in 2D polygonal networks, such that both ET as well as TE transition can be seen as combinations of triple T1 transitions of 4-polygon neighborhoods. In each T1 transition, a pair of initially neighboring polygons becomes separated, whereas polygons from the remaining (initially separated) polygon pair become neighbors. This suggests that, given an appropriate data representation, it should be possible to unify topological transformations in 2D and 3D space-filling packings. Consequently, implementing topological transformations in 3D polyhedral packings should be equally challenging than implementing T1 transitions 2D polygonal packings.

This observation directly contradicts the convoluted transformation algorithms from previous works on 3D cell aggregates and indicates the need for reformulating the vertex model's core architecture. The main challenge underlying this task is to find a data model of cell aggregates, in which topological transitions are performed by trivial data transformations, representing most elementary operations, that are apparently common in 2D and 3D models (Fig. 1d).

Results

Conventional vertex models are implemented over tabular data models, which are based on storing cell configurations in arrays. The main issue with this type of approach is that vertices, edges, polygons, and cells are stored in separate arrays (\mathbf{r}_i , \mathbf{e}_j , \mathbf{p}_k , and \mathbf{c}_l , respectively), which do not directly encode any interconnections or relationships among their respective elements. In particular, elements that might be spatially and topologically related are generally not stored together in the database and accessing any high-level topology data (e.g., finding cells that share a common vertex) requires inefficient searches over all the elements of the cell network.

To avoid these inefficient searches, the conventional vertex models store data in a highly redundant form, where higher-level information about the topology of the cell network are stored in addition to \underline{e}_j , \underline{p}_k , and \underline{c}_l (even though these higher-level information may be calculable from \underline{e}_j , \underline{p}_k , and \underline{c}_l). For instance, to efficiently search for cells that share a certain vertex, lists of cells sharing a common vertex need to be stored for all vertices. Indeed, retrieving this information from \underline{e}_j , \underline{p}_k , and \underline{c}_l on the fly would require highly inefficient looping over all the cells. Due to this data redundancy, algorithms that manipulate the data arrays upon topological transformations in a self-consistent manner are difficult to program.

Knowledge graph. To overcome these issues, we propose a new approach, based on storing the topology of the cell network into a knowledge graph, which uses a graph- rather than a tabular data model. By construction, the elements that are topologically related are also connected in the knowledge graph and therefore, any high-level information about the topology of the cell network is readily retrievable by querying over the relevant part of the database with no need of storing any redundant data.

Knowledge graph is a graph data structure, which represents a network of real-world entities and relationships between them [63]. These data are stored in a graph database where entities and relationships are represented by nodes and links, respectively, and can, additionally, carry multiple properties. For example, a movie database can be stored as a knowledge graph, in which the data about actors and directors for a given movie are represented by nodes labeled `Person` and `Movie` and relationships labeled `ACTED_IN` and `DIRECTED`. In such a knowledge graph, the information that Cillian Murphy acted in the movie *Oppenheimer*, directed by Christopher Nolan, can be stored as `(p1:Person {name: "Cillian Murphy"})-[:ACTED_IN]->(m:Movie {title: "Oppenheimer"})<-[:DIRECTED]-(p2:Person {name: "Christopher Nolan"})`; here nodes labeled `Person` and `Movie` carry the `name` and the `title` properties, respectively.

The notation used here and in the following sections follows the syntax of the `Cypher` graph query language [64]. It is important to note that GVM relies on general principles of discrete mathematics and does not depend neither on the choice of the query language nor on the choice of the database-management framework.

Metagraph. Real-world entities in GVM are vertices, edges, polygons, and cells and they are stored in a knowledge graph in a hierarchical manner as nodes labeled `Vertex`, `Edge`, `Polygon`, and `Cell`, respectively. The topology of the cell network is encoded through relationships labeled `IS_PART_OF`. These relationships are directed and relate source-target node pairs, where the entity represented by the source node is always hierarchically one level below the entity represented by the target node.

For instance, if a specific polygon p contains a specific edge e , the nodes representing these two entities, i.e., (p) and (e) , are connected as `(e)-[:IS_PART_OF]->(p)`. Connecting equally labeled nodes (e.g., a pair of edges) is not allowed and neither is connecting nodes carrying labels that do not follow one another hierarchically (e.g., a vertex-polygon pair). For example, say that one of the polygon p 's vertices is vertex v . Rather than encoding the information that v is part of p directly by a `(v)-[:IS_PART_OF]->(p)` connection, this information is retrieved hierarchically from the connectivity of v and p through edges. In particular, if v is part of p , it is also necessarily shared by two edges that are both also part of p (say e_1 and e_2): `(v)-[:IS_PART_OF]->(e1)-[:IS_PART_OF]->(p)` and `(v)-[:IS_PART_OF]->(e2)-[:IS_PART_OF]->(p)`. An extra connection `(v)-[:IS_PART_OF]->(p)` would be redundant and is therefore forbidden in GVM, since these two subgraphs already imply that v is one of polygon p 's vertices.

The above rules for the construction of the GVM's knowledge graph can be conveniently represented by a graph, called *metagraph*. Much like metalanguage is a language that describes another language, metagraph is a graph that describes another graph and can be viewed as a blueprint for generating actual (valid) manifestations of that graph. From the above definitions, it is obvious that the metagraph of GVM is `(:Vertex)-[:IS_PART_OF]->(:Edge)-[:IS_PART_OF]->(:Polygon)-[:IS_PART_OF]->(:Cell)` (Fig. 2a).

Additionally, both nodes and relationships carry properties that encode additional knowledge about nodes and relationships. While nodes carry a property, `id`, which represents the identification numbers i , j , k , and l of vertices, edges, polygons, and cells, respectively, the relationships are prescribed a property `sign`, whose value is either -1 or $+1$. This is a contextual property, that puts the relationship's source node into the context of the target node. In particular, in the subgraphs of type `(v:Vertex)-[r:IS_PART_OF]->(e:Edge)`, the value of `r.sign` denotes whether vertex v is a head vertex (`r.sign=+1`) or a tail vertex (`r.sign=-1`) of edge e [i.e., parameter s in Eq. (2)]. In the subgraphs of types `(e:Edge)-[r:IS_PART_OF]->(p:Polygon)` and `(p:Polygon)-[r:IS_PART_OF]->(c:Cell)` the same property specifies the orientation of edge e in the context of polygon p and polygon p in the context of cell c , respectively [i.e., parameters σ and Σ in Eqs. (3)

and (4), respectively].

Pattern matching. Transforming the graph database of GVM upon cell rearrangements requires only two steps: (i) Data retrieval, accomplished through pattern matching and (ii) Graph transformation. In step (i), a suitable (meta)graph pattern is utilized to query the database and identify the nodes relevant to the transformation at hand. After the graph is traversed, instances of the specified graph pattern are returned. If needed, these instances can be further filtered, using various conditional statements. For example, in an EV transition on edge i , the nodes representing polygons p_1 , p_2 , and p_3 (Fig. 1c) are found by a short query, shown in Eq. (18).

The goal of step (i) is to retrieve from the whole graph of GVM a small subgraph comprising solely of the nodes representing the objects (vertices, edges, polygons, and cells) that take part in the specific topological transformation being performed (Fig. 2b). Given the unambiguous definition of the graph data structure by the GVM's metagraph (Fig. 2a), the routines that perform this step are easily reproducible. We implement these routines in `Cypher` and find that each topological transition requires ~ 10 distinct short queries, similar to the query shown in Eq. (18) [52] to retrieve the relevant data.

Graph transformations. In step (ii), the subgraph matched during the pattern-matching step undergoes a transformation based on the rules of the specific cell-rearrangement event being performed.

Like the matched subgraph that is being transformed, the graph transformation itself is represented by a graph. This graph contains exactly the same nodes as the matched GVM subgraph, however with much fewer relationships. In particular, the relationships in the transformation graph are of two types: (i) Green and (ii) red, indicating creations and deletions of `:IS_PART_OF` relationships in the actual GVM subgraph, respectively (Fig. 2c).

For instance, a green relationship between nodes representing vertex v_1 and edge e_3 indicates creation of a new relationship between previously matched nodes (`v1`) and (`e3`) [Eq. (19)]. Similarly, a red relationship between edge e_5 and polygon p_4 , for example, indicates deletion of the relationship between previously matched nodes (`e5`) and (`p4`) [Eq. (20)]. Figure 3 shows graph transformations for ET and TE transformations as well as the matched subgraphs representing initial and final cell configurations. Graph transformations for EV, VT, TV, and VE transformations are given in Figs. S1 and S2. For clarity, the graphs representing all three states (E, T, and V) are additionally specified in a more explicit (non-pictorial) form in Methods.

Compared to the convoluted codes that perform topological transformations in the conventional vertex model, the task of programming the routines that perform topological transformations in GVM is much less challenging. Indeed, our implementation of graph-transformation routines in `Cypher` comprises of successive calls of ~ 5 distinct short queries, similar to examples shown in Eqs. (19) and (20).

Transformation of contextual properties. Values of contextual properties s , σ , and Σ to be assigned to the newly created relationships are specified in the transformation graph through the relationship property of green relationships (s' , σ' , and Σ' for vertex \rightarrow edge, edge \rightarrow polygon, and polygon \rightarrow cell connections, respectively). Unlike the green relationships, the red relationships do not carry any additional properties (Fig. 2c).

Contextual properties of the newly created relationships are easily calculable and are exactly specified in Fig. 3. In particular, for a new vertex \rightarrow edge relationship between nodes representing vertex v_i and edge e_j , $s'_{i,j}$ is calculated as

$$s'_{i,j} = s_{k,j}, \quad (6)$$

where k denotes vertex v_k , which was part of edge e_j prior to the transformation (i.e., $s_{k,j}$ denotes contextual property of the relationship between nodes representing vertex v_k and edge e_j prior to the transformation).

For a new edge \rightarrow polygon relationship between nodes representing edge e_i and polygon p_j , $\sigma'_{i,j}$ is calculated as

$$\sigma'_{i,j} = -s'_{k,i}s'_{k,l}\sigma_{l,j}. \quad (7)$$

Here, vertex v_k is a vertex shared by edges e_i and e_l , which are both part of polygon p_j . Additionally, among the two vertices of edge e_i , vertex v_k is the one that was not part of edge e_l prior to the transformation (i.e., Eq. (7) contains $s'_{k,l}$ and not $s_{k,l}$). An analogous equation to Eq. (7) also holds for assigning $\Sigma'_{i,j}$ to a newly created polygon \rightarrow cell relationship (i.e., $\Sigma'_{10,4}$ in Fig. 3a).

Note that values of contextual properties of certain newly created relationships need not be calculated, but can be either chosen arbitrarily or their values are automatically imposed (Fig. 3).

Generalization of topological transformations. In agreement with our observation that topological transformations in 3D polyhedral packings are composites of more elementary topological (T1) transformations in 2D polygonal networks (Fig. 1d), we find that graph transformations $\mathbf{T}_{\text{ET}}^{(3\text{D})}$ and $\mathbf{T}_{\text{TE}}^{(3\text{D})}$ both contain transformation patterns corresponding to T1 transitions (Fig. 4 and Fig. S3). This result generalizes ET and TE topological transformations to "multidimensional" T1 transitions.

Moreover, both $\mathbf{T}_{\text{ET}}^{(3\text{D})}$ and $\mathbf{T}_{\text{TE}}^{(3\text{D})}$ simplify to a single T1 transition when applied to an edge in a polygonal network (Fig. 4). Even though $\mathbf{T}_{\text{ET}}^{(3\text{D})}$ and $\mathbf{T}_{\text{TE}}^{(3\text{D})}$ both assume the input subgraph of a form with 5 cell nodes, 10 polygon nodes, 9 edge nodes, and 3 vertex nodes, exactly the same transformations can be applied to a subgraph representing a 4-polygon neighborhood in a 2D polygonal packing, undergoing a T1 transition. In this case, the pattern-matching step only matches 2 vertices, 5 edges, and 4 polygons and only a subset of graph-transformation operations (4 relationship creations, 4 relationship deletions, and 6 property assignments) are performed (Fig. 4 and Fig. S3). This result unifies topological transformations in 2D and 3D systems, suggesting that GVM's data structure may be the most natural representation of space-filling polyhedral packings.

Active tissue fluidization. As a proof of concept, we develop a custom Python package called `neoVM`, which manages the GVM's knowledge graph and its transformations in a graph database management framework Neo4j (Methods).

We use `neoVM`, to study fluidization of cell aggregates by active tension fluctuations. In particular, we consider an aggregate of $N_c = 128$ cells, enclosed within a simulation box with periodic boundary conditions. The vertex dynamics are described by Eq. (5), assuming the potential energy given by Eq. (10). In addition to the conservative and friction forces, we also include active force dipoles acting along cell edges to induce active cell rearrangements. The total active force on vertex i is a sum of forces acting along edges (i.e., tricellular junctions) sharing that same vertex:

$$\mathbf{F}_i^{(a)} = - \sum_{lmn} \gamma_{lmn}(t) \nabla_i L_{lmn}. \quad (8)$$

Here the indices lmn denote a tricellular junction (i.e., edge), shared by cells l , m , and n ; L_{lmn} is the edge length.

The magnitudes of active force dipoles are dynamic quantities that fluctuate with time. In particular $\gamma_{lmn}(t)$ obeys Ornstein-Uhlenbeck dynamics described by

$$\dot{\gamma}_{lmn}(t) = -\frac{1}{\tau_m} (\gamma_{lmn}(t) - \gamma_0) + \xi_{lmn}(t), \quad (9)$$

where τ_m is the relaxation time scale associated with turnover dynamics of molecular motor Myosin, γ_0 is a baseline tension, whereas $\xi_{lmn}(t)$ is Gaussian white noise with properties $\langle \xi_{lmn}(t) \rangle = 0$ and $\langle \xi_{lmn}(t) \xi_{opr}(t') \rangle = (2\sigma^2/\tau_m) \delta_{io} \delta_{mp} \delta_{nr} \delta(t - t')$; σ^2 is the long-time variance of the tension fluctuations.

We simulate the above active dynamics at different magnitudes of active noise σ , starting with a Kelvin structure—a crystalline cell arrangement made up of truncated octahedra with 14 facets (8 regular hexagons and 6 squares). The active noise distorts the geometry of the aggregates, which are no longer perfect crystals. In particular, for $\sigma > 0$ the average cell shape, quantified by the shape factor $q = \langle S_i/V_i^{2/3} \rangle_{i \in \text{cells}}$ (S_i and V_i are cell surface area and volume, respectively) deviates from the Kelvin's truncated octahedron (Fig. 5a). The distorted geometry is also seen in the width of the distribution of edge lengths, which increases with an increasing σ —to a point where vanishingly short edges appear (Fig. 5b). These edges undergo ET and TE topological transformations, which in turn triggers cell rearrangements—a signature of a transition from a solid- to a fluid-like behavior. This transition is seen in the dependence of an order parameter $1 - f_{14}$, describing the fraction of non-14-sided polyhedra ($f_{14} = N_{14}/N_c$), on the control parameter σ (Fig. 5c). From these results, we obtain an estimate for the transition point $\sigma^* \approx 0.17$. Figs. 5d-h show cell configurations at $\sigma = 0, 0.2, 0.3, 0.4$, and 0.5 .

Next, we are interested in whether the active noise can drive the opposite effect, i.e., ordering. To study this, we start with a disordered cell packing, prepared in advance by packing spheres in the simulation box, using random sequential addition and then constructing Voronoi partitions around sphere centers. This procedure yields a sample with the initial fraction of 14-sided polyhedra $f_{14} = 0.234$. Again, we simulate the active dynamics at different magnitudes of the active noise σ . We find that high- σ values keep the

aggregate disordered due to frequent cell-neighbor exchanges. In contrast, a sufficiently small level of active noise drives active tissue ordering, which is seen in decreasing $1 - f_{14}$ and narrowing of the edge-length distribution over time (Fig. 5i and Fig. 5j, respectively). At moderate $\sigma \approx \sigma^*$ values, the ordering is more efficient compared to small σ values, where the active-noise level is not sufficient to allow overcoming local energy barriers for cell rearrangements. Despite a higher degree of disorder, the low- σ states consist of cells whose shapes are closer to the Kelvin’s regular truncated octahedron compared to cells from the $\sigma \approx \sigma^*$ case, where cell shapes are perturbed due to active noise (Fig. 5k).

The rate of topological-transition events in the simulations of active cell aggregates reaches as high as ~ 200 /time unit, which in total amounts to $\sim 10^5$ events per simulation (Fig. 5c); note that many of these events are reversible transitions that occur multiple times while the manipulated vertices are still located very close to one another and have not yet properly resolved in geometric sense. Despite this large number of reconnections, the aggregate keeps its integrity, demonstrating that topological transformations in space-filling 3D packings can indeed be implemented as graph transformations defined in Figs. 3 and 4. Importantly, due to GVM’s unambiguous data structure, these transformations are relatively straight-forward to implement and are therefore readily reproducible, which is clearly demonstrated by the implementation of GVM within our `neoVM` package [52].

Discussion. We reformulated the vertex model of cell aggregates. The new formulation, called Graph Vertex Model (GVM), is based on storing the topology of the cell network into a knowledge graph. We discovered a particular graph data model, uniquely defined by a metagraph, which allows formulating topological transformations of the cell network as simple and mathematically properly defined graph transformations (Fig. 2). These transformations are themselves represented by graphs and consist of only the most elementary graph operations, i.e., node and relationship deletions and creations.

We designed graph transformations for all topological transitions, required to describe cell rearrangements—including edge-to-triangle (ET) and triangle-to-edge (TE) transformations (Fig. 3). We showed that ET and TE transformations are inherently of the same type since they are both merely composites of transformation patterns corresponding to T1 transitions (Fig. 4). Importantly, when applied to a 2D system, both ET and TE transformations reduce to a single T1 transition, thereby unifying topological transformations in 2D and 3D space-filling packings (Fig. 4). These fundamental insights surfaced due to the particular graph data structure of GVM, which seems to be the most natural representation of the topology of space-filling packings. We used GVM to study active cell aggregates, whose cell junctions are subject to fluctuating active tensions (Fig. 5). In particular, we characterized the solid-to-fluid transition and found disordered aggregates undergoing ordering, which is most efficient for active noise close to the transition point.

Our work represents a pioneering effort in introducing graph databases into the fields of tissue mechanics and biology. Even though the basic GVM’s data model presented here only encodes information on the topology of cell networks, GVM already represents an important technological and conceptual step forward in computational models of tissue mechanics. This advancement lays the foundation for the creation of knowledge graphs capable of structurally storing live-imaging data, such as that obtained from developing embryos. This involves integrating data on geometry, topology, mechanics, and biochemistry. With this aim, our ongoing work uses GVM as a starting point to develop a comprehensive knowledge-graph database of the early fly development [65]. By making this database interactive and accessible online will allow collaborative research with the aim to progressively expand our collective knowledge base about the mechanics of the embryonic development. Additionally, its graph data structure may even be readily complemented with graph-compatible methods of artificial intelligence (e.g., Graph Neural Networks).

In the context of computational modelling, a considerable effort will also have to be devoted to developing technologies that will improve computational efficiency of the vertex-model simulations over a graph database. While our current implementation of GVM, `neoVM` [52], primarily serves as a proof of concept, it falls short on the efficiency. The reason for this is mostly twofold: (i) The time integration of the dynamical system is performed in `Python`, which is generally slower than some low-level programming languages, and (ii) Performing operations on the graph database managed by `Neo4j` necessitates reading from and writing to the local hard drive, where the database is stored. The latter could be improved by relying on the memory storage instead.

Methods

Calculation of forces. We neglect the inertial effects so that the friction force $\mathbf{F}_i^{(f)}$ needs to counterbalance the sum of conservative and active forces, $\mathbf{F}_i^{(c)}$ and $\mathbf{F}_i^{(a)}$, respectively. This implies $\mathbf{F}_i^{(f)} + \mathbf{F}_i^{(c)} + \mathbf{F}_i^{(a)} = 0$, where the conservative force $\mathbf{F}_i^{(c)} = -\nabla_i W$, with W being the potential energy of the system, whereas $\mathbf{F}_i^{(f)} = -\eta \dot{\mathbf{r}}_i$. Here, only friction with a static (“ether-type”) background is considered, η being the associated friction coefficient. The active force $\mathbf{F}_i^{(a)}$ can describe different system-specific active mechanisms, e.g., active contractions of the cell membrane due to the activity of the underlying cell cortex or traction forces [19, 20, 32, 54]. This model yields a system of first-order dynamic equations for vertex positions given by Eq. (5).

We consider a model, in which cell-cell interfaces are prescribed by effective surface tensions Γ_{lm} , which include contributions of the cell cortical tension and cell-cell adhesion [55–57]; the notation lm denotes index of a polygon shared by cells l and m . In this model, the total potential energy of the cell aggregate reads

$$W = \sum_{\langle lm \rangle} \Gamma_{lm} A_{lm} + \kappa_V \sum_l (V_l - V_0)^2, \quad (10)$$

where the first sum goes over all pairs of neighboring cells l and m and the second sum goes over all the cells, κ_V and V_0 being the cell-incompressibility constant and the preferred cell volume, respectively.

By definition, the conservative force acting on vertex i is calculated as

$$\mathbf{F}_i^{(c)} = - \sum_{\langle lm \rangle} \Gamma_{lm} \nabla_i A_{lm} - 2\kappa_V \sum_l (V_l - V_0) \nabla_i V_l, \quad (11)$$

which further requires calculating gradients of interfacial surface areas and cell volumes as described below.

Surface area of polygonal side k is calculated as a sum of surface areas of triangular surface elements, $\|\mathbf{a}_{lm,\mu}\|$, defined by pairs of consecutive polygon vertices \mathbf{r}_μ and $\mathbf{r}_{\mu+1}$, and the polygon’s center of mass

$$\mathbf{c}_{lm} = \frac{1}{n_{lm}} \sum_{\mu \in \langle lm \rangle} \mathbf{r}_\mu. \quad (12)$$

Like in the previous section, Greek indices here do not denote the real vertex identification numbers, but their sequential indices within individual polygons. The surface area of polygon lm reads

$$A_{lm} = \sum_{\mu \in \langle lm \rangle} \frac{1}{2} \|\mathbf{r}_\mu - \mathbf{c}_{lm}\| \times \|\mathbf{r}_{\mu+1} - \mathbf{c}_{lm}\| \quad (13)$$

and its gradient

$$\nabla_i A_{lm} = \sum_{\mu \in \langle lm \rangle} \frac{1}{2} \nabla_i \|\mathbf{r}_\mu - \mathbf{c}_{lm}\| \times \|\mathbf{r}_{\mu+1} - \mathbf{c}_{lm}\| = \quad (14)$$

$$= \sum_{\mu \in \langle lm \rangle} \frac{[(\delta_{i\mu} - n_{lm}^{-1})(\mathbf{r}_{\mu+1} - \mathbf{c}_{lm}) + (n_{lm}^{-1} - \delta_{i(\mu+1)})(\mathbf{r}_\mu - \mathbf{c}_{lm})] \times \mathbf{a}_{lm,\mu}}{4\|\mathbf{a}_{lm,\mu}\|}, \quad (15)$$

where δ_{ij} is the Kronecker delta.

Cell volume l is calculated as a sum of volumes of tetrahedra, defined by triangular surface elements $(\mathbf{r}_\mu, \mathbf{r}_{\mu+1}, \mathbf{c}_{lm})$ and with the fourth vertex at the origin $(0, 0, 0)$, as

$$V_l = \sum_m \sum_{\mu \in \langle lm \rangle} \frac{1}{6} \mathbf{c}_{lm} \cdot (\mathbf{r}_\mu \times \mathbf{r}_{\mu+1}). \quad (16)$$

Its gradient is calculated as

$$\nabla_i V_l = \sum_m \sum_{\mu \in \langle lm \rangle} \frac{1}{6} \nabla_i [\mathbf{c}_{lm} \cdot (\mathbf{r}_\mu \times \mathbf{r}_{\mu+1})] = \sum_m \sum_{\mu \in \langle lm \rangle} \frac{1}{6n_{lm}} (\mathbf{r}_\mu \times \mathbf{r}_{\mu+1}) + \frac{1}{6} (\delta_{i\mu} \mathbf{r}_{\mu+1} - \delta_{i(\mu+1)} \mathbf{r}_\mu) \times \mathbf{c}_{lm}. \quad (17)$$

Topological transformations. None of the topological transitions is allowed if the resulting cell configuration breaks any of the following topological rules [44, 50]: (i) Edge pairs may not share more than one vertex, (ii) polygon pairs may not share more than one edge and (iii) cell pairs may not share more than one polygon.

Cypher queries for pattern matching and graph transformations. The following Cypher query retrieves nodes representing the polygons that share common edge i

```
MATCH (e:Edge)
WHERE e.id=i
MATCH (e)-[:IS_PART_OF]->(p:Polygon)
RETURN p
```

(18)

The following Cypher query creates a new relationship IS_PART_OF between nodes (v1) and (e3) and assigns property value s23.

```
CREATE (v1)-[:IS_PART_OF {sign:$s23}]->(e3)
```

(19)

The following Cypher query deletes relationship r between nodes (e5) and (p4).

```
MATCH (e5)-[r:IS_PART_OF]->(p4)
DELETE r
```

(20)

List of relationships. For clarity, we here explicitly list relationships in graphs representing states E, T, and V (Figs. 3 and 4 and Figs. S1 and S2). All relationships are of type IS_PART_OF.

- **[state E]:** $v_1 \rightarrow e_1, v_1 \rightarrow e_2, v_1 \rightarrow e_5, v_1 \rightarrow e_7, v_2 \rightarrow e_3, v_2 \rightarrow e_4, v_2 \rightarrow e_6, v_2 \rightarrow e_7, e_1 \rightarrow p_1, e_1 \rightarrow p_4, e_1 \rightarrow p_8, e_2 \rightarrow p_2, e_2 \rightarrow p_4, e_2 \rightarrow p_6, e_3 \rightarrow p_1, e_3 \rightarrow p_5, e_3 \rightarrow p_9, e_4 \rightarrow p_2, e_4 \rightarrow p_5, e_4 \rightarrow p_7, e_5 \rightarrow p_3, e_5 \rightarrow p_6, e_5 \rightarrow p_8, e_6 \rightarrow p_3, e_6 \rightarrow p_7, e_6 \rightarrow p_9, e_7 \rightarrow p_1, e_7 \rightarrow p_2, e_7 \rightarrow p_3, p_1 \rightarrow c_1, p_1 \rightarrow c_2, p_2 \rightarrow c_1, p_2 \rightarrow c_3, p_3 \rightarrow c_2, p_3 \rightarrow c_3, p_4 \rightarrow c_1, p_4 \rightarrow c_4, p_5 \rightarrow c_1, p_5 \rightarrow c_5, p_6 \rightarrow c_3, p_6 \rightarrow c_4, p_7 \rightarrow c_3, p_7 \rightarrow c_5, p_8 \rightarrow c_2, p_8 \rightarrow c_4, p_9 \rightarrow c_2, p_9 \rightarrow c_5$
- **[state T]:** $v_1 \rightarrow e_1, v_1 \rightarrow e_3, v_1 \rightarrow e_7, v_1 \rightarrow e_9, v_2 \rightarrow e_2, v_2 \rightarrow e_4, v_2 \rightarrow e_7, v_2 \rightarrow e_8, v_3 \rightarrow e_5, v_3 \rightarrow e_6, v_3 \rightarrow e_8, v_3 \rightarrow e_9, e_1 \rightarrow p_1, e_1 \rightarrow p_4, e_1 \rightarrow p_8, e_2 \rightarrow p_2, e_2 \rightarrow p_4, e_2 \rightarrow p_6, e_3 \rightarrow p_1, e_3 \rightarrow p_5, e_3 \rightarrow p_9, e_4 \rightarrow p_2, e_4 \rightarrow p_5, e_4 \rightarrow p_7, e_5 \rightarrow p_3, e_5 \rightarrow p_6, e_5 \rightarrow p_8, e_6 \rightarrow p_3, e_6 \rightarrow p_7, e_6 \rightarrow p_9, e_7 \rightarrow p_4, e_7 \rightarrow p_5, e_7 \rightarrow p_{10}, e_8 \rightarrow p_6, e_8 \rightarrow p_7, e_8 \rightarrow p_{10}, e_9 \rightarrow p_8, e_9 \rightarrow p_9, e_9 \rightarrow p_{10}, p_1 \rightarrow c_1, p_1 \rightarrow c_2, p_2 \rightarrow c_1, p_2 \rightarrow c_3, p_3 \rightarrow c_2, p_3 \rightarrow c_3, p_4 \rightarrow c_1, p_4 \rightarrow c_4, p_5 \rightarrow c_1, p_5 \rightarrow c_5, p_6 \rightarrow c_3, p_6 \rightarrow c_4, p_7 \rightarrow c_3, p_7 \rightarrow c_5, p_8 \rightarrow c_2, p_8 \rightarrow c_4, p_9 \rightarrow c_2, p_9 \rightarrow c_5, p_{10} \rightarrow c_4, p_{10} \rightarrow c_5$
- **[state V]:** $v_1 \rightarrow e_1, v_1 \rightarrow e_2, v_1 \rightarrow e_3, v_1 \rightarrow e_4, v_1 \rightarrow e_5, v_1 \rightarrow e_6, e_1 \rightarrow p_1, e_1 \rightarrow p_4, e_1 \rightarrow p_8, e_2 \rightarrow p_2, e_2 \rightarrow p_4, e_2 \rightarrow p_6, e_3 \rightarrow p_1, e_3 \rightarrow p_5, e_3 \rightarrow p_9, e_4 \rightarrow p_2, e_4 \rightarrow p_5, e_4 \rightarrow p_7, e_5 \rightarrow p_3, e_5 \rightarrow p_6, e_5 \rightarrow p_8, e_6 \rightarrow p_3, e_6 \rightarrow p_7, e_6 \rightarrow p_9, p_1 \rightarrow c_1, p_1 \rightarrow c_2, p_2 \rightarrow c_1, p_2 \rightarrow c_3, p_3 \rightarrow c_2, p_3 \rightarrow c_3, p_4 \rightarrow c_1, p_4 \rightarrow c_4, p_5 \rightarrow c_1, p_5 \rightarrow c_5, p_6 \rightarrow c_3, p_6 \rightarrow c_4, p_7 \rightarrow c_3, p_7 \rightarrow c_5, p_8 \rightarrow c_2, p_8 \rightarrow c_4, p_9 \rightarrow c_2, p_9 \rightarrow c_5$

Implementation in Python and Neo4j. As a proof of concept, we set up the GVM’s knowledge-graph database in a graph database management framework Neo4j [53]. The core program of the vertex model is implemented in Python and communicates with Neo4j using Py2neo client library. The time integration of the dynamical system is performed in Python, whereas all topological transformations are performed in Neo4j through pattern matching and graph transformations implemented as Cypher queries [64]. Our implementation of GVM is available as an open-source Python package, called neoVM, and is available online [52].

Figure S4 shows the schematic of neoVM’s architecture. The program is initialized by reading the initial geometry and topology of the cell network from an input .vt3d file and storing them into an object \mathbf{t} of class **tissue**. In particular, this object stores lists of **vertex**, **edge**, **polygon**, and **cell** objects, which encode \mathbf{r}_i , \mathbf{e}_j , \mathbf{p}_k , and \mathbf{c}_l , respectively, in a tabular form. This is followed by generating an object \mathbf{db} of class **database**, which connects to an empty Neo4j database and fills it with the tissue data according to the rules of the GVM’s metagraph, using function `setup_DB()`.

The initialization is followed by a time loop, which propagates the system forward in time by time steps Δt . At each time step, the dynamical system [Eq. (5)] is integrated between t and $t + \Delta t$ [function `solver()`] and the program checks whether any of the edges in the cell network meets conditions for topological transitions [function `topological_transitions()`]. In particular, edge j undergoes an ET transition if it is shorter than a threshold length l_{th} and the rate of change of its length is negative ($dl_j/dt < 0$), i.e., the edge is contracting. If the edge happens to be part of a triangle, a TE transition is performed on the triangle if, additionally, all edges of the triangle are shorter than l_{th} and the area of the triangle is decreasing ($dA_k/dt < 0$).

For every edge/triangle, subject to a topological transition, the core program sends a sequence of `Cypher` queries to the `Neo4j` graph database. These queries (i) perform pattern matching to isolate a subgraph relevant for the particular transformation being performed, and (ii) perform graph transformation on that subgraph. After graph transformations, vertex positions are displaced such that the lengths of the newly created edges (edges e_7 , e_8 , and e_9 in Fig. 1) are on the order of $l_{new} \ll 1$. Finally, the local structure of the arrays, encoding \underline{r}_i , \underline{e}_j , \underline{p}_k , and \underline{c}_l , (stored in object `t`) are updated according to the applied transformations. This is done by converting the altered part of the knowledge graph back into the array format using function `update()`.

Data availability

Data supporting the findings of this manuscript are available from the corresponding author upon reasonable request. `neoVM` is available in an online repository [52]. A reporting summary for this Article is available as a Supplementary Information file.

References

- [1] T. Lecuit and P.-F. Lenne, *Cell surface mechanics and the control of cell shape, tissue patterns and morphogenesis*, *Nat. Rev. Mol. Cell Biol.* **8**, 633 (2007).
- [2] T. E. Angelini, E. Hannezo, X. Trepant, M. Marquez, J. J. Fredberg, and D. A. Weitz, *Glass-like dynamics of collective cell migration*, *Proc. Natl. Acad. Sci. USA* **108**, 4714 (2011).
- [3] J.-A. Park *et al.*, *Unjamming and cell shape in the asthmatic airway epithelium*, *Nat. Mater.* **14**, 1040 (2015).
- [4] A. Mongera, P. Rowghanian, H. J. Gustafson, E. Shelton, D. A. Kealhofer, E. K. Carn, F. Serwane, A. A. Lucio, J. Giammona, and O. Campàs, *A fluid-to-solid jamming transition underlies vertebrate body axis elongation*, *Nature* **561**, 401 (2018).
- [5] R. Etournay, M. Popović, M. Merkel, A. Nandi, C. Blasse, B. Aigouy, H. Brandl, G. Myers, G. Salbreux, F. Jülicher, and S. Eaton, *Interplay of cell dynamics and epithelial tension during morphogenesis of the Drosophila pupal wing*, *eLife* **4**, e07090 (2015).
- [6] D. E. Discher, P. Janmey, and Y.-L. Wang, *Tissue Cells Feel and Respond to the Stiffness of Their Substrate*, *Science* **310**, 1139 (2005).
- [7] V. F. Fiore, M. Krajnc, F. Garcia Quiroz, J. Levorse, H. A. Pasolli, S. Y. Shvartsman, and E. Fuchs, *Mechanics of a multilayer epithelium instruct tumour architecture and function*, *Nature* **585**, 433 (2020).
- [8] J. T. Blankenship, S. T. Backovic, J. S. P. Sanny, O. Weitz, and J. A. Zallen, *Multicellular rosette formation links planar cell polarity to tissue morphogenesis*, *Dev. Cell* **11**, 459 (2006).
- [9] A. Martin, M. Kaschube, and E. F. Wieschaus, *Pulsed contractions of an actin-myosin network drive apical constriction*, *Nature* **457**, 459 (2009).
- [10] M. Rauzi, U. Krzic, T. E. Saunders, M. Krajnc, P. Zihler, L. Hufnagel, and M. Leptin, *Embryo-scale tissue mechanics during Drosophila gastrulation movements*, *Nat. Commun.* **6**, 8677 (2015).

- [11] S. Streichan, M. F. Lefebvre, N. Noll, E. F. Wieschaus, and B. I. Shraiman, *Global morphogenetic flow is accurately predicted by the spatial distribution of myosin motors*, *eLife* **7**, e27454 (2018).
- [12] T. Stern, S. Y. Shvartsman, and E. F. Wieschaus, *Template-based mapping of dynamic motifs in tissue morphogenesis*, *PLoS Comput. Biol.* **16**, e1008049 (2020).
- [13] T. Stern, S. Y. Shvartsman, and E. F. Wieschaus, *Deconstructing gastrulation at single-cell resolution*, *Curr. Biol.* **32**, 1861 (2022).
- [14] C. Bertet, L. Sulak, and T. Lecuit, *Myosin-dependent junction remodelling controls planar cell intercalation and axis elongation*, *Nature* **429**, 667 (2004).
- [15] M. Rauzi, P. Verant, T. Lecuit, and P.-F. Lenne, *Nature and anisotropy of cortical forces orienting Drosophila tissue morphogenesis*, *Nat. Cell Biol.* **10**, 1401 (2008).
- [16] M. Rauzi, P.-F. Lenne, and T. Lecuit, *Planar polarized actomyosin contractile flows control epithelial junction remodelling*, *Nature* **468**, 1110 (2010).
- [17] T. Lecuit, P.-F. Lenne, E. Munro, *Force generation, transmission, and integration during cell and tissue morphogenesis*, *Annu. Rev. Cell Dev. Biol.* **27**, 157 (2011).
- [18] T. Lecuit and A. S. Yap, *E-cadherin junctions as active mechanical integrators in tissue dynamics*, *Nat. Cell Biol.* **17**, 533 (2015).
- [19] S. Curran, C. Strandkvist, J. Bathmann, M. de Gennes, A. Kabla, G. Salbreux, and B. Baum, *Myosin II Controls Junction Fluctuations to Guide Epithelial Tissue Ordering*, *Dev. Cell* **43**, 480 (2017).
- [20] M. Krajnc, *Solid–fluid transition and cell sorting in epithelia with junctional tension fluctuations*, *Soft Matter* **13**, 3209 (2020).
- [21] M. Krajnc, S. Dasgupta, P. Ziherl, and J. Prost, *Fluidization of epithelial sheets by active cell rearrangements*, *Phys. Rev. E* **98**, 022409 (2018).
- [22] M. Krajnc, T. Stern, and C. Zankoc, *Active Instability and Nonlinear Dynamics of Cell-Cell Junctions*, *Phys. Rev. Lett.* **127**, 198103 (2021).
- [23] M. F. Staddon, K. E. Cavanaugh, E. M. Munro, M. L. Gardel, and S. Banerjee, *Mechanosensitive junction remodeling promotes robust epithelial morphogenesis*, *Biophys. J.* **19**, 1739 (2019).
- [24] K. E. Cavanaugh, M. F. Staddon, T. A. Chmiel, R. Harmon, S. Budnar, S. Banerjee, and M. L. Gardel, *Force-dependent intercellular adhesion strengthening underlies asymmetric adherens junction contraction*, *Curr. Biol.* **32**, 1986 (2022).
- [25] R. Sknepnek, I. Djafer-Cherif, M. Chuai, C. Weijer, and S. Henkes, *Generating active T1 transitions through mechanochemical feedback*, *eLife* **12**, e79862 (2023).
- [26] R. Alert and X. Trepat, *Physical Models of Collective Cell Migration*, *Annu. Rev. Condens. Matter Phys.* **11**, 77 (2020).
- [27] F. Graner, J. A. Glazier, *Simulation of biological cell sorting using a two-dimensional extended Potts model*, *Phys. Rev. Lett.* **69**, 2013 (1992).
- [28] J. A. Glazier and F. Graner, *Simulation of the differential adhesion driven rearrangement of biological cells*, *Phys. Rev. E* **47**, 2128 (1993).
- [29] M. H. Swat, G. L. Thomas, J. M. Belmonte, A. Shirinifard, D. Hmeljak, and J. A. Glazier, *Multi-scale modeling of tissues using CompuCell3D*, *Methods Cell Biol.* **110**, 325 (2012).
- [30] D. Bi, J. H. Lopez, J. M. Schwarz, and M. L. Manning, *A density-independent glass transition in biological tissues*, *Nat. Phys.* **11**, 1074 (2015).

- [31] M. Misra, B. Audoly, I. G. Kevrekidis, and S. Y. Shvartsman, *Biophys. J.* **110**, 1670 (2016).
- [32] D. Bi, X. Yang, M. C. Marchetti, and M. L. Manning, *Motility-driven glass and jamming transitions in biological tissues*, *Phys. Rev. X* **6**, 021011 (2016).
- [33] D. L. Barton, S. Henkes, C. J. Weijer, and R. Sknepnek, *Active vertex model for cell-resolution description of epithelial tissue mechanics*, *PLoS Comp. Biol.* **13**, e1005569 (2017).
- [34] R. Mueller, J. M. Yeomans, and A. Doostmohammadi, *Emergence of Active Nematic Behavior in Monolayers of Isotropic Cells*, *Phys. Rev. Lett.* **122**, 048004 (2019).
- [35] S. Kim, M. Pochitaloff, G. A. Stooke-Vaughan, and O. Campàs, *Embryonic tissues as active foams*, *Nat. Phys.* **17**, 859 (2021).
- [36] H. Honda, M. Tenemura, and T. Nagai, *A three-dimensional vertex dynamics cell model of space-filling polyhedra simulating cell behavior in a cell aggregate*, *J. Theor. Biol.* **226**, 439 (2004).
- [37] R. Farhadifar, J. C. Röper, B. Aigouy, S. Eaton, and F. Jülicher, *The influence of cell mechanics, cell-cell interactions, and proliferation on epithelial packing*, *Curr. Biol.* **17**, 2095 (2007).
- [38] A. G. Fletcher, M. Osterfield, R. E. Baker, and S. Y. Shvartsman, *Vertex models of epithelial morphogenesis*, *Biophys. J.* **106**, 2291 (2014).
- [39] S. Alt, P. Ganguly, and G. Salbreux, *Vertex models: from cell mechanics to tissue morphogenesis*, *Philos. Trans. R. Soc. Lond. B Biol. Sci.* **372**, 20150520 (2017).
- [40] <https://github.com/DamCB/tyssue>.
- [41] G. R. Mirams, C. J. Arthurs, M. O. Bernabeu, R. Bordas, J. Cooper, A. Corrias, Y. Davit, S.-J. Dunn, A. G. Fletcher, D. G. Harvey *et al.*, *Chaste: An open source C++ library for computational physiology and biology*, *PLoS Comput. Biol.* **9**, e1002970 (2013).
- [42] D. M. Sussman, *cellGPU: Massively parallel simulations of dynamic vertex models*, *Comput. Phys. Commun.* **219**, 400 (2017).
- [43] <https://github.com/ZhangTao-SJTU/tvm>.
- [44] S. Okuda, Y. Inoue, M. Eiraku, Y. Sasai, and T. Adachi, *Reversible network reconnection model for simulating large deformation in dynamic tissue morphogenesis*, *Biomech. Model. Mechanobiol.* **12**, 627 (2013).
- [45] S. Okuda, T. Miura, Y. Inoue, T. Adachi, and M. Eiraku, *Combining turing and 3D vertex models reproduces autonomous multicellular morphogenesis with undulation, tubulation, and branching*, *Sci. Rep.* **8**, 2386 (2018).
- [46] L. Sui, S. Alt, M. Weigert, N. Dye, S. Eaton, F. Jug, E. W. Myers, F. Jülicher, G. Salbreux, and C. Dahmann, *Differential lateral and basal tension drive folding of Drosophila wing discs through two distinct mechanisms*, *Nat. Commun.* **9**, 4620 (2018).
- [47] J. Rozman, M. Krajnc, and P. Zihlerl, *Collective cell mechanics of epithelial shells with organoid-like morphologies*, *Nat. Commun.* **11**, 3805 (2020).
- [48] J. Rozman, M. Krajnc, and P. Zihlerl, *Morphologies of compressed active epithelial monolayers*, *Eur. Phys. J. E* **44**, 1 (2021).
- [49] S. Okuda and K. Sato, *Polarized interfacial tension induces collective migration of cells, as a cluster, in a 3D tissue*, *Biophys. J.* **121**, 1856 (2022).
- [50] T. Zhang and J. M. Schwarz, *Topologically-protected interior for three-dimensional confluent cellular collectives*, *Phys. Rev. Res.* **4**, 043148 (2022).

- [51] E. Lawson-Keister, Tao Zhang, and M. L. Manning, *Differences in boundary behavior in the 3D vertex and Voronoi models*, arXiv: 2306.03987.
- [52] <https://gitlab.com/ijskrajncgroup1/neo4j>.
- [53] <https://neo4j.com/product>.
- [54] X. Trepap, M. R. Wasserman, T. E. Anglelini, E. Millet, D. A. Weitz, J. P. Butler, and J. J. Fredberg, *Physical forces during collective cell migration*, *Nat. Phys.* **5**, 426 (2009).
- [55] J. Derganc, S. Svetina, and B. Žekš, *Equilibrium mechanics of monolayered epithelium*, *J. Theor. Biol.* **260**, 333 (2009).
- [56] M. L. Manning, R. A. Foty, M. S. Steinberg, and E.-M. Schoetz, *Coaction of intercellular adhesion and cortical tension specifies tissue surface tension*, *Proc. Natl. Acad. Sci. USA* **107**, 12517 (2010).
- [57] E. Hannezo, J. Prost, and J.-F. Joanny, *Theory of epithelial sheet morphology in three dimensions*, *Proc. Natl. Acad. Sci. USA* **111**, 27 (2013).
- [58] D. Weaire and M. A. Fortes, *Networklike Propagation of Cell-Level Stress in Sheared Random Foams*, *Adv. Phys.* **43**, 685 (1994).
- [59] D. A. Reinelt and A. M. Kraynik, *Simple shearing flow of a dry Kelvin soap foam*, *J. Fluid Mech.* **311**, 327 (1996).
- [60] H. W. Schwarz, *Rearrangements in polyhedral foam*, *Recl. Trav. Chim. Pays-Bas* **84**, 771 (1965).
- [61] J.-F. Rupprecht, K. H. Ong, J. Yin, A. Huang, A. P. Singh, S. Zhang, W. Yu, T. E. Saunders, *Geometric constraints alter cell arrangements within curved epithelial tissues*, *Mol. Biol. Cell* **28**, 3582 (2017).
- [62] P. Gómez Gálvez *et al.*, *Scutoids are a geometrical solution to three-dimensional packing of epithelia*, *Nat. Commun.* **9**, 2960 (2018).
- [63] H. Paulheim, *Knowledge Graph Refinement: A Survey of Approaches and Evaluation Methods*, *Semant. Web* **8**, 489 (2017).
- [64] https://neo4j.com/docs/cypher-manual/current/introduction/cypher_overview/.
- [65] M. Krajnc, J. Deuser, J. Lampič, T. Sarkar, and T. Stern, *In preparation*.

Author Contributions

M.K. conceived the project; T.S. and M.K. developed graph transformations; T.S. carried out the numerical work; T.S. analyzed the data; T.S. and M.K. wrote the paper.

Acknowledgments

We thank Tomer Stern, Domen Vaupotič, Staš Adam, and all members of the Theoretical Biophysics Group at Jožef Stefan Institute for fruitful discussions. The main idea for this project surfaced from a very fruitful collaboration with Wisdom Labs. Thanks to all Wisdom Labs folks, especially Andraž Tuš, Kristjan Pečanac, Luka Stopar, Marko Zadavec, Jasna Pečanac, and Jan Lampič. We acknowledge the financial support from the Slovenian Research Agency (research project No. J1-3009 and research core funding No. P1-0055).

Competing interests

The authors declare no competing interests.

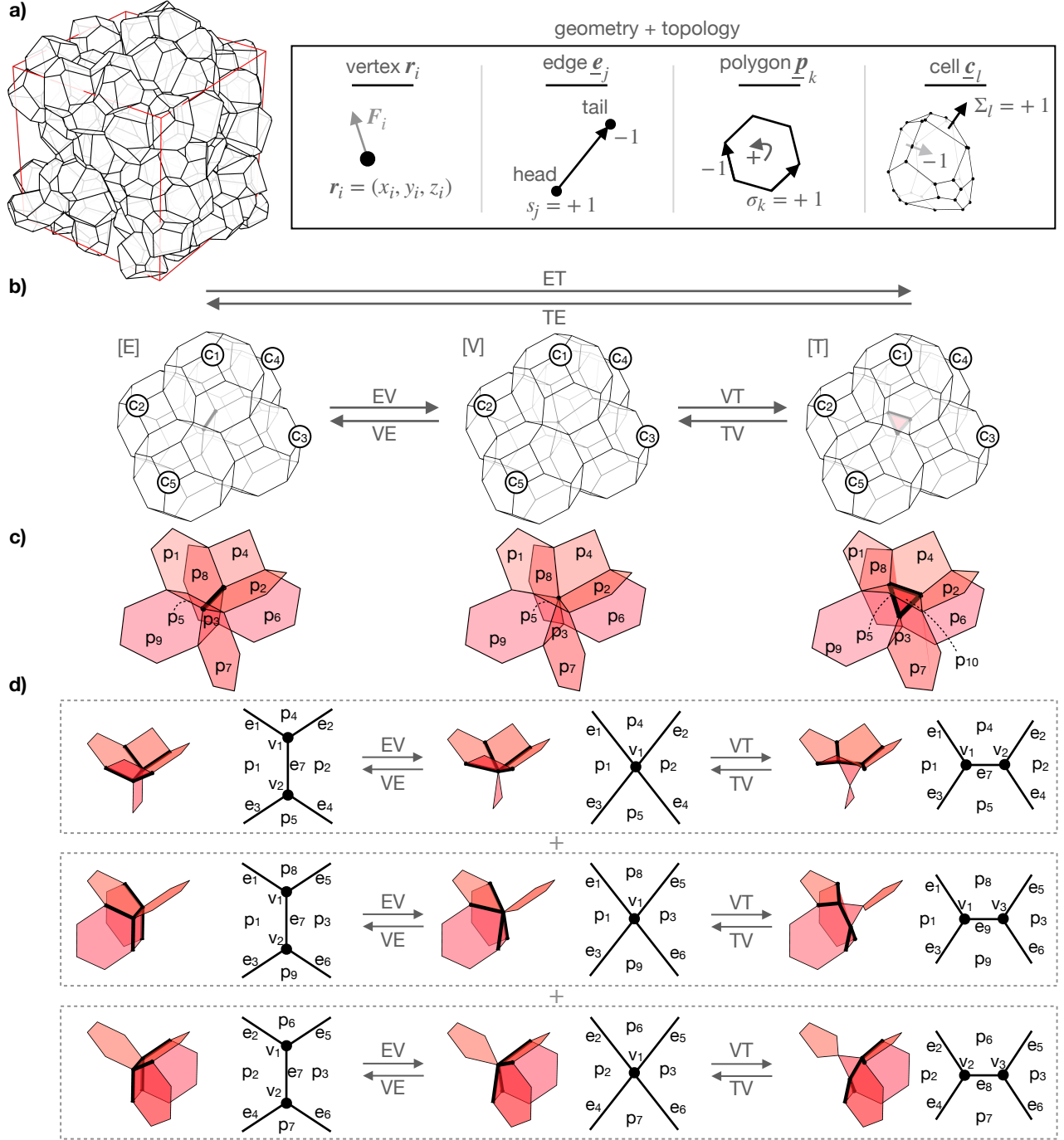


Figure 1: Geometry and topology of cell aggregates. **a** Cell aggregate is modeled by a space-filling packing of polyhedral cells. Cell shapes are parametrized by vertex positions \mathbf{r}_i , which move according to mechanical forces \mathbf{F}_i . Topology of the cell network is specified by lists \underline{e}_j , \underline{p}_k , and \underline{c}_l [Eqs. (2)-(4)], which store head and tail vertices of edges, oriented edges within polygons, and oriented polygons within cells, respectively. **b** EV transition merges vertices of an edge into a single vertex, whereas VT transition resolves a vertex into a triangle. TV and VE transitions are inverse transitions of EV and VT transitions, respectively. **c** Polygons involved in topological transitions from panel b. **d** Polygons and edges involved in topological transitions from panel b. 3D topological transitions can be viewed as triple 2D topological transitions, where only edges and polygons are involved.

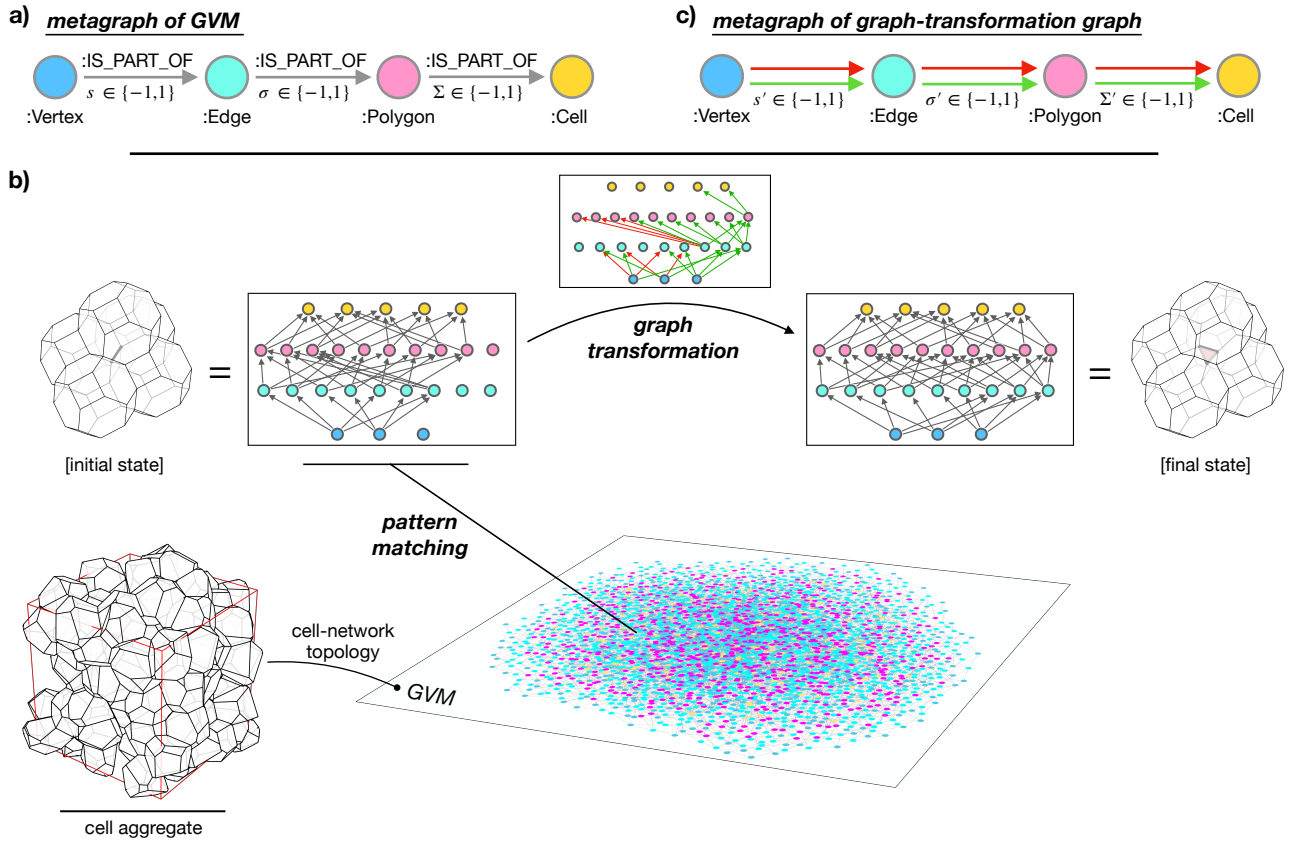


Figure 2: Graph Vertex Model. **a** The hierarchical structure of GVM vertex→edge→polygon→cell is defined by a metagraph. Relationships between these nodes are labeled `IS_PART_OF` and carry a **sign** property denoted by s , σ , and Σ for vertex→edge, edge→polygon, and polygon→cell relationships, respectively. **b** Pattern matching a subgraph representing a particular local cell state, subject to a rearrangement event. This graph is then transformed by a graph transformation. **c** Metagraph of graph-transformation graph connects `Vertex`, `Edge`, `Polygon`, and `Cell` nodes with green and red relationships, indicating creation and deletion of `IS_PART_OF` relationships in the GVM’s knowledge graph.

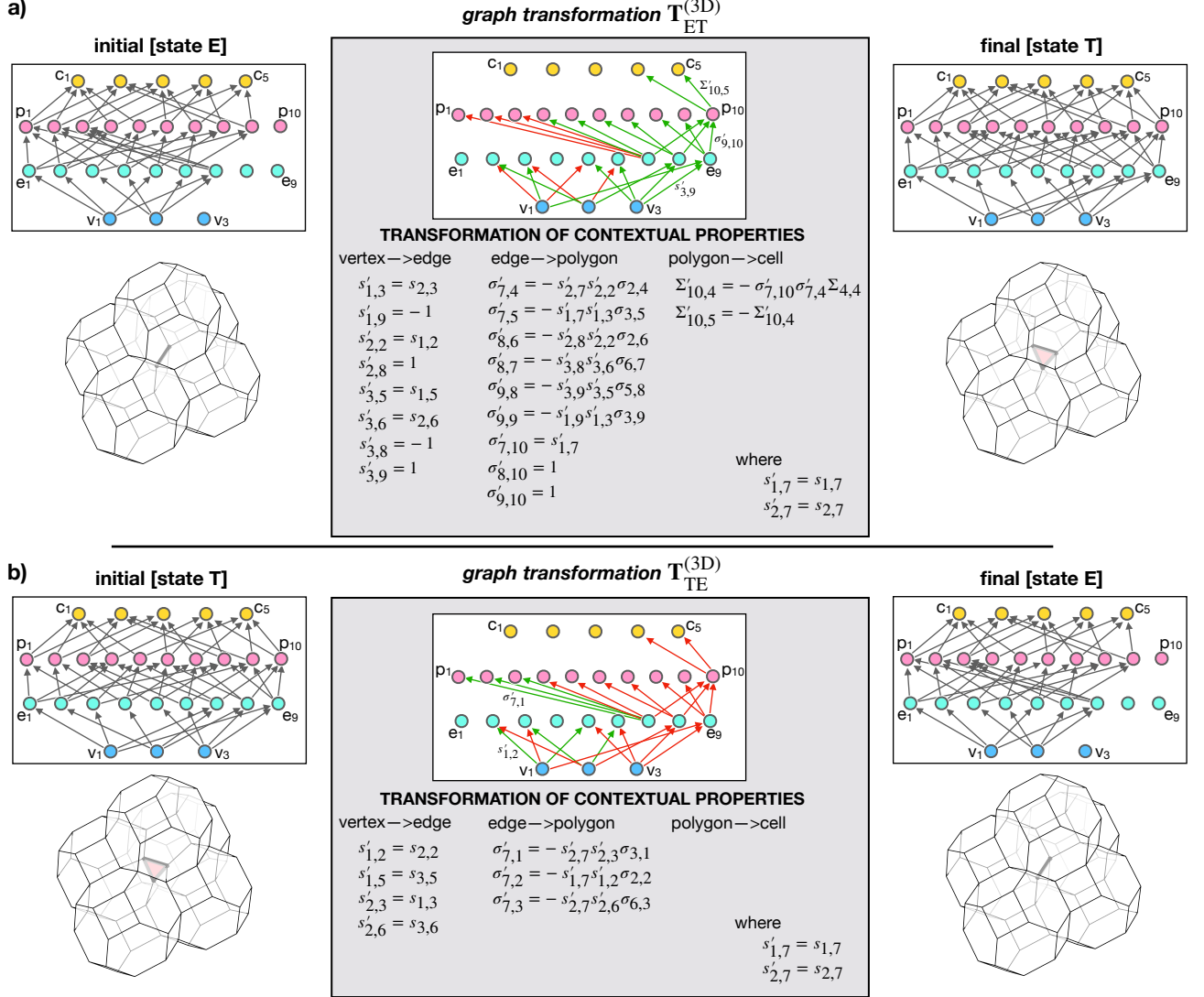


Figure 3: Graph transformations in a 3D vertex model of polyhedral packings. **a** Graph transformation of an ET transition. **b** Graph transformation of an TE transition. In both panels, graphs in the left and the right column correspond to the initial and the final cell configuration, respectively. Gray arrows represent relationships labeled IS_PART_OF. The graphs in the middle column show graph transformations, which include green and red relationships, indicating relationship creations and deletions, respectively. Additionally, the graph transformation specifies property values of the newly created relationships. In each graph, the node indices increase from left to right in unit steps.

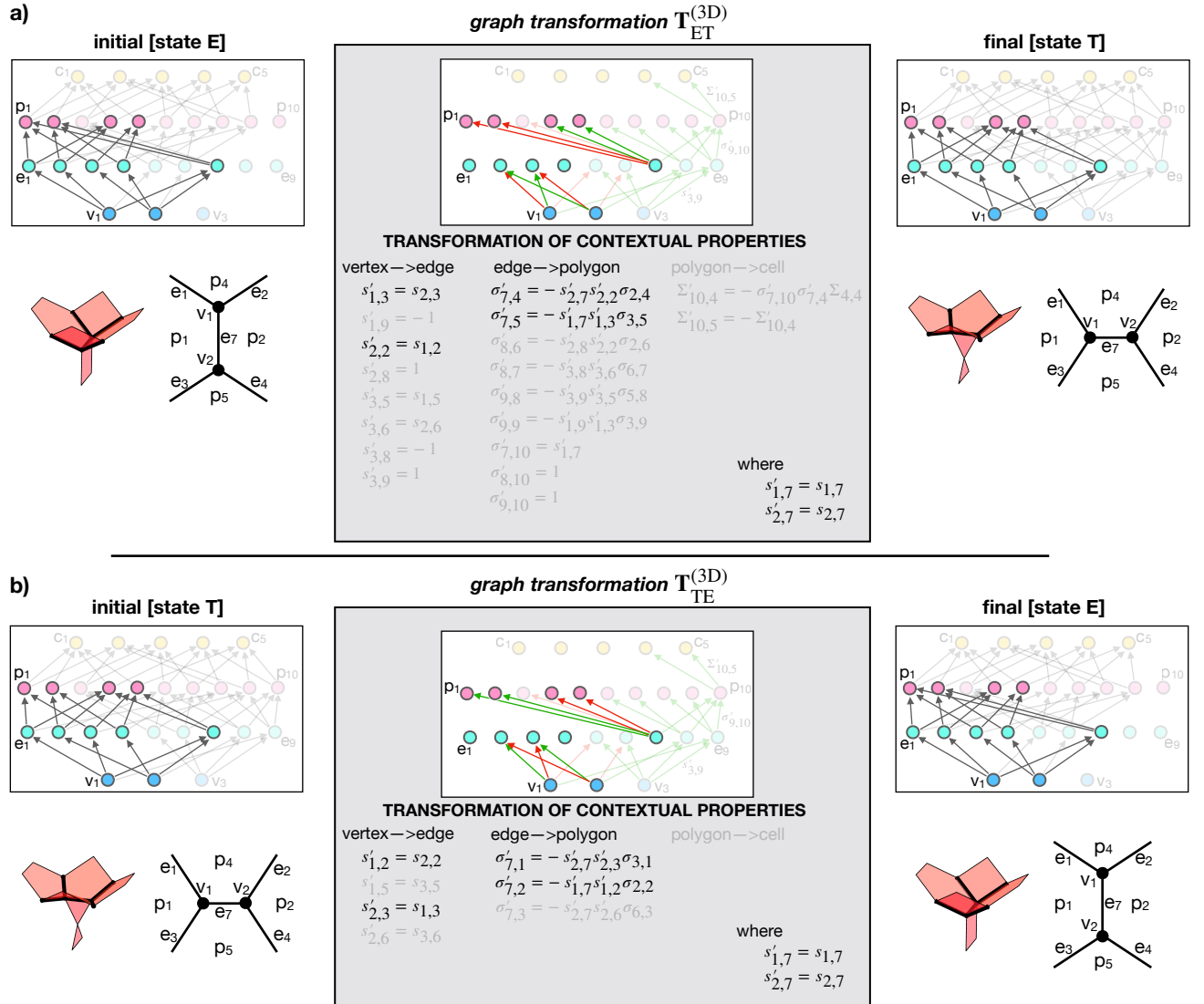


Figure 4: Graph transformations of ET and TE transitions reduce to a T1 transition. **a** ET transformation when applied to a four-polygon neighborhood. **b** TE transformation when applied to a four-polygon neighborhood. In both panels, those nodes and relationships from the original ET and TE transformations (Fig. 3) that are not matched are displayed transparent. The remaining opaque, i.e., matched, nodes and relationships exactly describe a T1 transformation. This shows that ET and TE transformations contain common transformation patterns, representing composites of T1 transitions, thereby unifying transformations in 2D and 3D space-filling packings. Graph transformation of a T1 transition contains 2 vertex \rightarrow edge relationship deletions, 2 vertex \rightarrow edge relationship creations, 2 edge \rightarrow polygon relationship deletions, and 2 edge \rightarrow polygon relationship creations (Fig. S3).

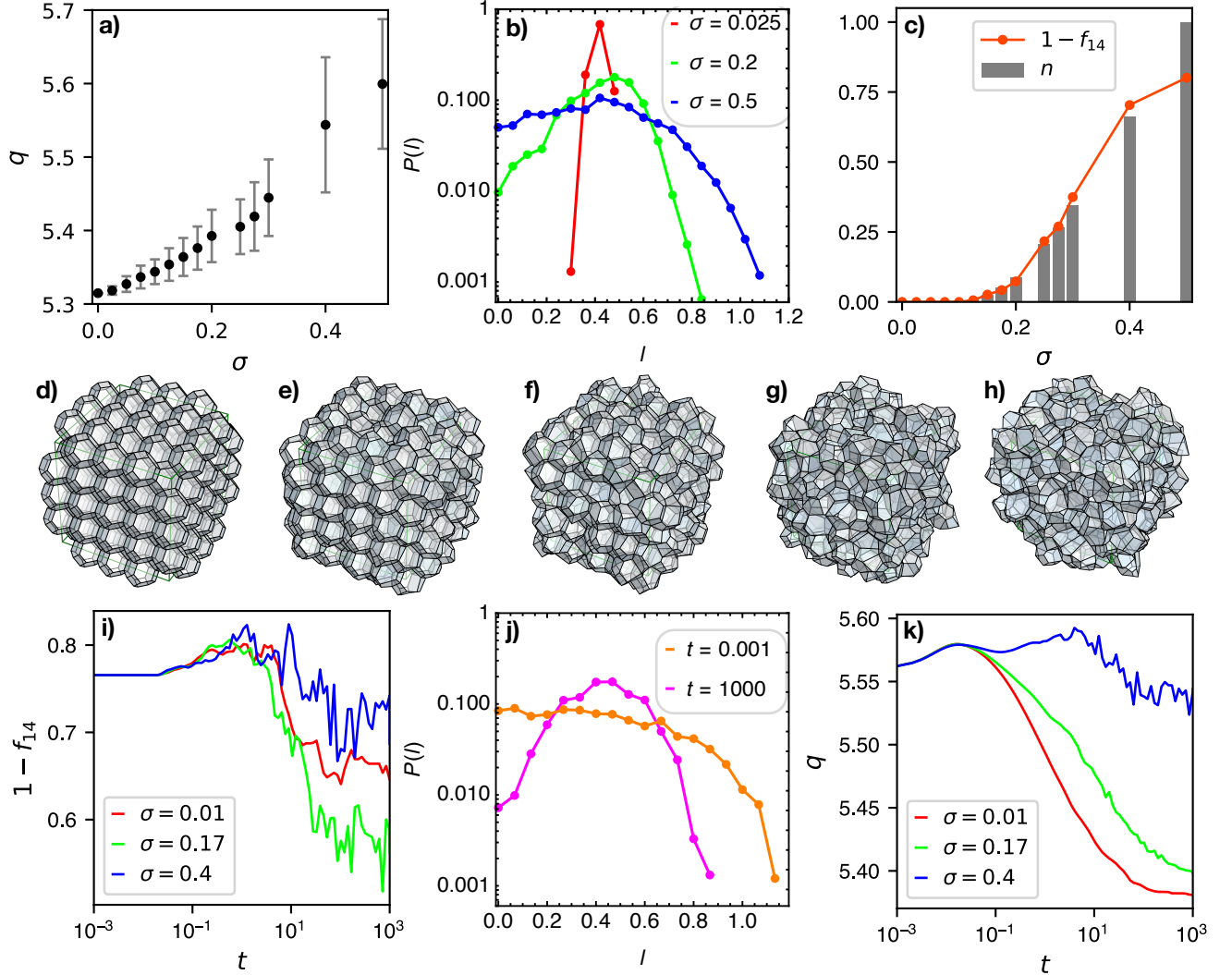


Figure 5: Solid-fluid transition in 3D cell aggregates. **a** Shape parameter q for “thermalized” aggregates versus active noise σ . **b** Distribution of edge lengths in thermalized aggregates for $\sigma = 0.025, 0.2$, and 0.5 (red, green, and blue curves, respectively). **c** Order parameter $1 - f_{14}$ and normalized number of cell-rearrangement events $n = (N_{ET} + N_{TE})/N_{\max}$ versus active noise σ . **d-h** Thermalized aggregates at $\sigma = 0, 0.2, 0.3, 0.4$, and 0.5 . **i** Order parameter $1 - f_{14}$ versus time for $\sigma = 0.01, 0.17$ and 0.4 (red, green, and blue curves, respectively) during aggregate ordering. **j** The initial ($t = 0.001$; orange curve) and final ($t = 1000$; magenta curve) distributions of edge lengths at $\sigma = 0.17$. **k** Shape parameter q versus time for $\sigma = 0.01, 0.17$ and 0.4 (red, green, and blue curves, respectively) during aggregate ordering.

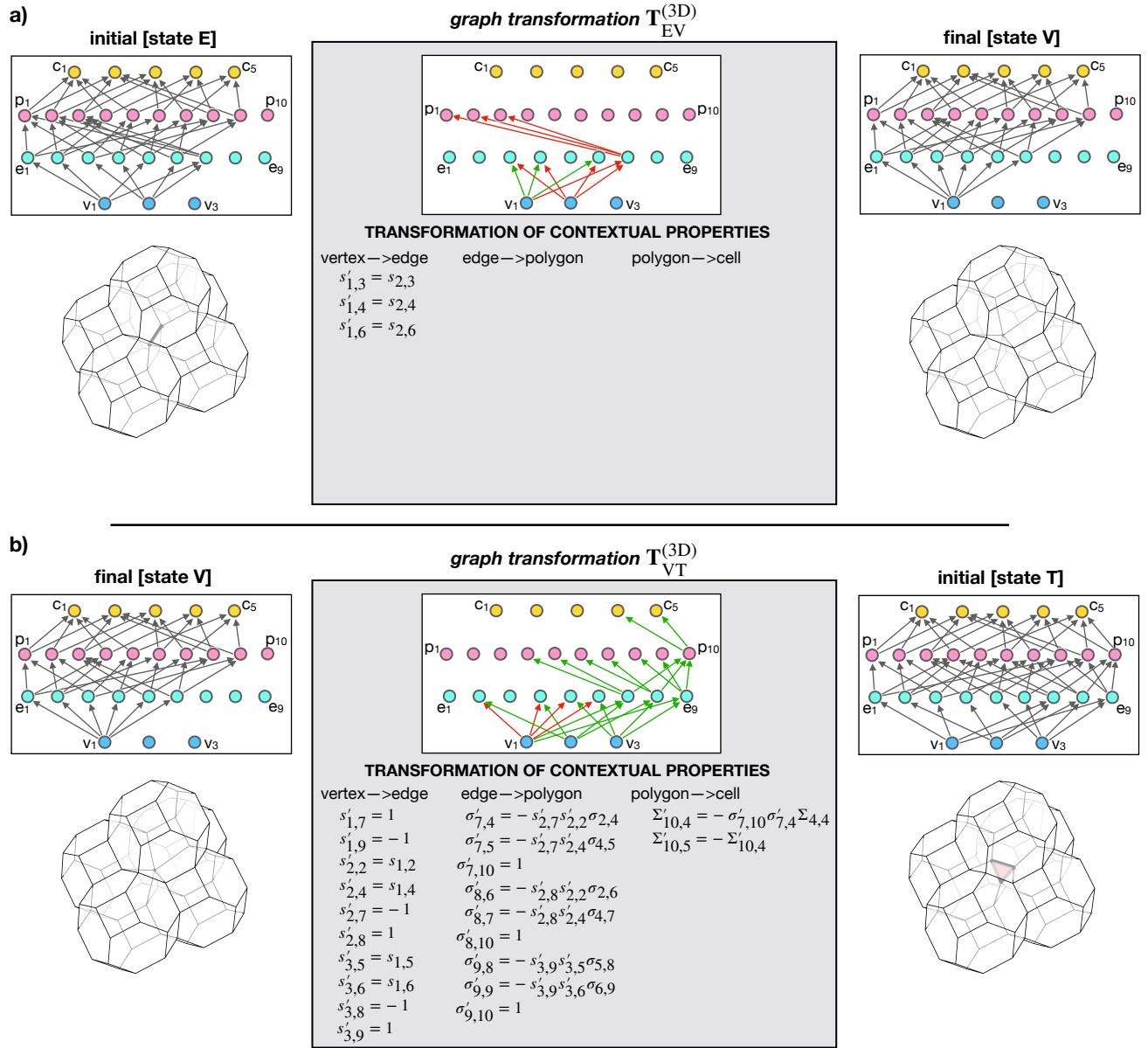


Figure S1: Graph transformations of EV and VT transitions . (panels a and b, respectively). Graphs in the left and the right column correspond to the initial and the final cell configuration, respectively. Gray arrows represent relationships labeled IS_PART_OF. The graphs in the middle column show graph transformations, which include green and red relationships, indicating relationship creations and deletions, respectively. Additionally, the graph transformation specifies property values of the newly created relationships. In each graph, the node indices increase from left to right in unit steps.

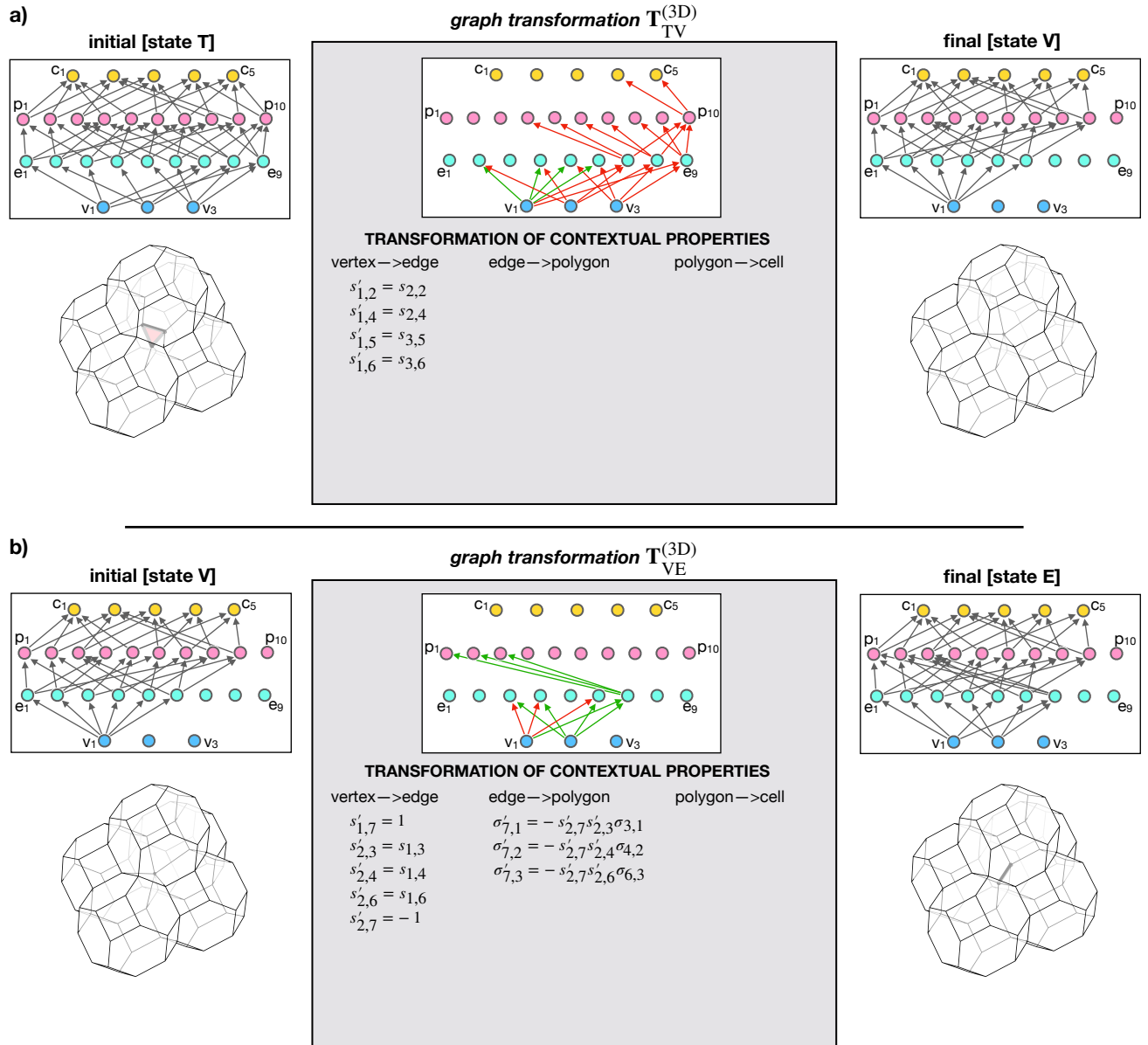


Figure S2: Graph transformations of TV and VE transitions. (panels a and b, respectively). Graphs in the left and the right column correspond to the initial and the final cell configuration, respectively. Gray arrows represent relationships labeled IS_PART_OF. The graphs in the middle column show graph transformations, which include green and red relationships, indicating relationship creations and deletions, respectively. Additionally, the graph transformation specifies property values of the newly created relationships. In each graph, the node indices increase from left to right in unit steps.

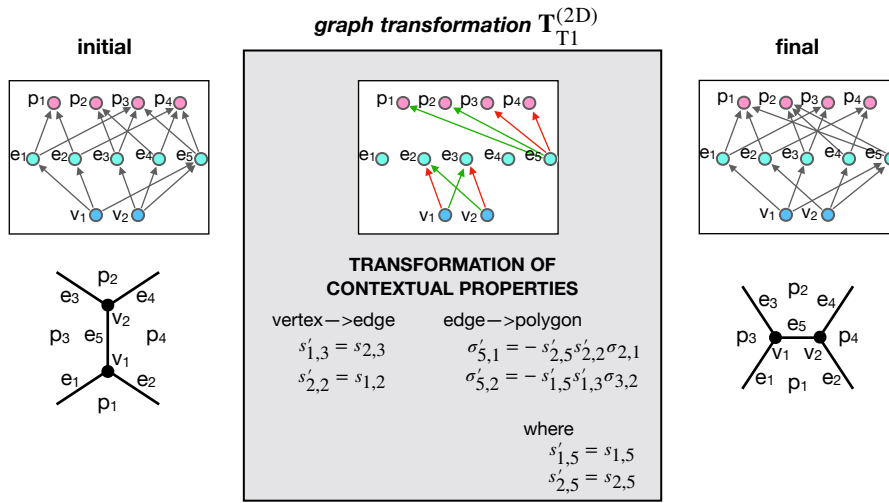


Figure S3: Graph transformation for a T1 transition. Graphs in the left and the right column correspond to the initial and the final cell configuration, respectively. Gray arrows represent relationships labeled IS_PART_OF. The graph in the middle column shows the graph transformation, which includes green and red relationships, indicating relationship creations and deletions, respectively. Additionally, the graph transformation specifies property values of the newly created relationships. In each graph, the node indices increase from left to right in unit steps.

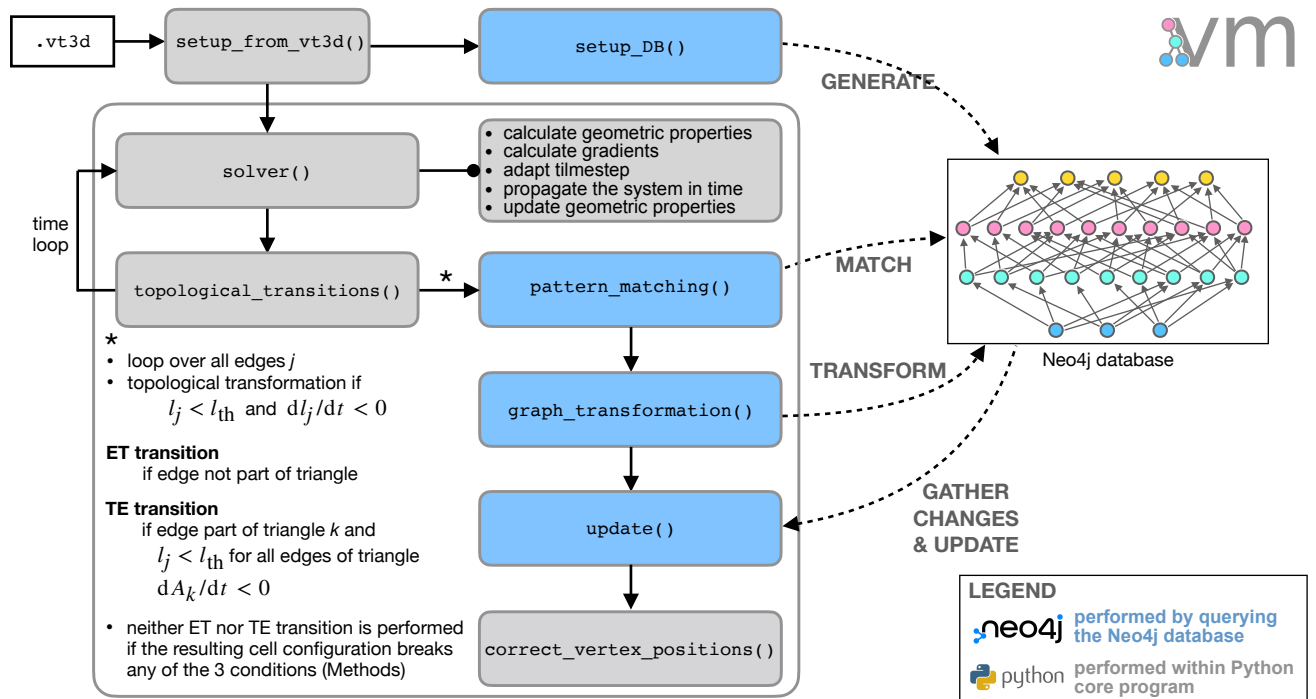


Figure S4: The algorithm underlying neoVM. A 3D cell aggregate is set up from an input `.vt3d` file by function `setup_from_vt3d()` and then converted into a graph database, set up in Neo4j by function `setupDB()`. These initialization steps then followed by a time loop, which iterates between `solver()` and `topological_transitions()` functions. The function `solver()` calculates geometric properties of cells and the associated gradients (i.e., conservative forces) and propagates the system forward in time. The function `topological_transitions()` loops over all cell edges to find those that meet criteria for topological transitions. For edges that meet these criteria, topological transitions are performed through pattern matching and graph transformations (functions `pattern_matching()` and `graph_transformation()`, respectively), applied directly to the graph database. Finally, the tissue is updated accordingly by function `update()` and positions of vertices involved in the topological transformation are corrected by function `correct_vertex_positions()`.